ACSNANO

www.acsnano.org

ARTICLE

Strain in Copper/Ceria Heterostructure Promotes Electrosynthesis of Multicarbon Products

Haibin Wang, Hao Zhang, Yan Huang, Haiyu Wang, Adnan Ozden, Kaili Yao, Huamin Li, Qianying Guo, Yongchang Liu, Alberto Vomiero, Yuhang Wang, Zhao Qian, Jun Li, Ziyun Wang, Xuhui Sun, and Hongyan Liang*

Cite This: *ACS Nano* 2023, 17, 346−354

Read Online

ACCESS | Metrics & More | Article Recommendations | Supporting Information

ABSTRACT: **Elastic strains in metallic catalysts induce enhanced selectivity for carbon dioxide reduction (CO_2R) toward valuable multicarbon (C_{2+}) products. However, under working conditions, the structure of catalysts inevitably undergoes reconstruction, hardly retaining the initial strain. Herein, we present a metal/metal oxide synthetic strategy to introduce and maintain the tensile strain in a copper/ceria heterostructure, enabled by the presence of a thin interface layer of Cu_2O/CeO_2. The tensile strain in the copper domain and deficient electron environment around interfacial Cu sites resulted in strengthened adsorption of carbonaceous intermediates and promoted *CO dimerization. The strain effect in the copper/ceria heterostructure leads to an improved C_{2+} selectivity with a maximum Faradaic efficiency of 76.4% and a half-cell power conversion efficiency of 49.1%. The fundamental insights gained from this system can facilitate the rational design of heterostructure catalysts for CO_2R.**

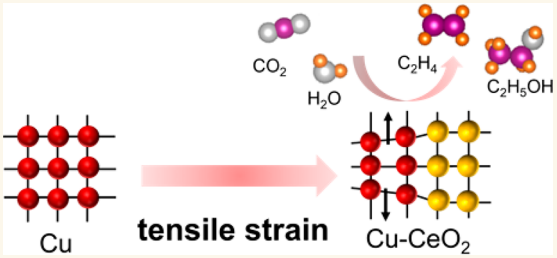

KEYWORDS: *tensile strain, copper/ceria heterostructure, electroreduction of carbon dioxide, synergistic effect, electrocatalyst*

INTRODUCTION

Electrocatalytic CO_2 reduction (CO_2R) to value-added chemicals and fuels using intermittent solar or wind electricity provides an ideal avenue to store renewable energy and close the carbon cycle.[1] During the CO_2R process, up to 16 different gas/liquid products can be achieved. The production of multicarbon (C_{2+}) hydrocarbons and alcohols, which are of higher value and have higher energy densities than single carbon (C_1) products, are highly attractive for commercial implementation.[2,3] To boost the C_{2+} production during CO_2R, great efforts have been made to explore efficient and selective catalysts.[4] Currently, Cu is the ideal catalyst with appreciable selectivity toward C_{2+} products.[5,6] Although recent progress has been made in facilitating C−C coupling over the C_1 pathway via various strategies, such as controlling the exposed facets,[7,8] introducing grain boundaries or defective interfaces,[9−11] stabilizing the oxidative Cu sites,[12−14] and constructing nanocavities,[15,16] the intrinsic feature of monometallic Cu limits the extent of improvement in selectivity for C_{2+}.[17−20]

Based on the Sabatier principle, the binding energies of carbonaceous intermediates affect the selectivity for C_{2+} production.[21] Introducing elastic strains in metallic catalysts can adjust their electronic structure and, in turn, the binding energies toward adsorbates, modulating the intrinsic features of the catalysts.[22,23] In CO_2R, the strain effect has a crucial impact on regulating the catalytic activity and selectivity.[19,24,25] For example, epitaxially grown Cu (001) film on Si substrate with a tunable tensile strain enhances the production of C_{2+} products due to a strengthened adsorbate−surface interaction.[21] CuAg bimetallic electrodes showed more selectivity for C_{2+} products than pure copper because of the compressive strain effect.[25] Strain in metallic catalysts is generally caused by lattice engineering, and the typical structures include core@shell or overlayer/substrate structure (wherein the two structures possess different lattice constants) and solid solution alloys (wherein the elemental components possess different atomic diameters).[22] However, under the negative potential and harsh electrochemical environment during CO_2R, the catalysts will undergo spontaneous reconstruction. The structural changes in

Received: August 23, 2022
Accepted: December 19, 2022
Published: December 27, 2022

https://doi.org/10.1021/acsnano.2c08453
ACS Nano 2023, 17, 346−354

working conditions, such as fragmentation, agglomeration, or phase separation, have been believed to degrade the original strain effect.

Recent studies have shown that constructing metal/metal oxide heterostructures is an efficient strategy to improve the dispersion or stability of the metallic sites.[26,27] Moreover, metal oxides can regulate the catalytic activity of catalysts via metal−metal oxide electronic interactions or direct participation in the electrochemical reaction.[5] However, the strain effect in metal/metal oxide heterostructures during CO_2R has been rarely exploited. Thus, we propose to tune the interfacial properties in a copper/metal oxide core/shell structure. This way, we are able to introduce strain into the copper domain and to prevent the copper from structural changes simultaneously, thus favoring selective CO_2R.

Herein, we fabricated the copper/ceria (CeO_2) heterostructure for CO_2R. We chose ceria because of its Pourbaix-stability under the reducing potentials.[28] Starting from a Cu_2O core/Cu_2O-CeO_2 shell nanocube, a hybrid structure was obtained for CO_2R. The large lattice spacing of ceria stretched Cu−O bonds and enlarged the Cu_2O lattice, which introduced tensile strain. During the CO_2R process, Cu_2O was reduced to Cu, and the tensile strain was maintained in metallic copper. Experimental measurements and density functional theory (DFT) simulations revealed that the tensile strain caused by lattice mismatch in copper domains strengthens the binding energy of *CO with Cu. The Cu-ceria interaction creates an electron-deficient environment around interfacial Cu sites, further enhancing the *CO adsorption and facilitating *CO dimerization. Moreover, ceria sites can accelerate water dissociation to feed sufficient protons for subsequent CO_2 conversion. Finally, a Cu/CeO_2 heterostructure with 4.4% tensile strain reached a Faradaic efficiency (FE) of 76.4% and a half-cell power conversion efficiency of 49.1% for C_{2+} products. This study deepens the mechanistic understanding of Cu/CeO_2 heterostructure catalysts during CO_2R and suggests successful strategies to develop high-performance catalysts based on elastic strain.

RESULTS AND DISCUSSION

We first investigated the strain effect of the Cu/CeO_2 heterostructure by building different DFT models for calculations (Figure 1). First, the binding energies of key intermediates *CO on the surface of Cu with and without tensile strain were calculated (Figure 1a). The *CO binding energy of standard Cu (111) was decreased when the tensile strain was introduced, which was further decreased with the addition of ceria forming the interface (Figure 1a and Table S1). Therefore, the stretched Cu domains in Cu/CeO_2 represent the best condition for binding *CO, consistent with the previous report.[21] Moreover, our DFT calculations found that the O atom of CeO_2 attracted electrons from the neighboring Cu, causing charge density rearrangement (Figure 1b). The deficient electron environment of copper contributed to further strengthen *CO adsorption.

In an alkaline electrolyte, water is the proton source for CO_2R. Previous reports claimed that the presence of ceria facilities water dissociation.[5] Our DFT studies also found that the Gibbs free energy (ΔG) for the cleavage of the H−OH bond (Figure 1c and Figure S1), the so-called Volmer step, is 0.34 eV on the Cu surface and 0.27 eV on the CeO_2 surface. The results indicate that water activation on CeO_2 is more favorable than on the Cu surface. Hence, the Cu/CeO_2 interface provides sufficient protons through accelerated water dissociation, leading to increased activity for CO_2R. Meanwhile, the enhancement of *H adsorption on the stretched Cu/CeO_2 interface is less than that of *CO adsorption, and thus the CO_2R is promoted rather than HER (Figure S2 and Table S1).[5] These findings motivated us to synthesize copper/ceria catalysts.

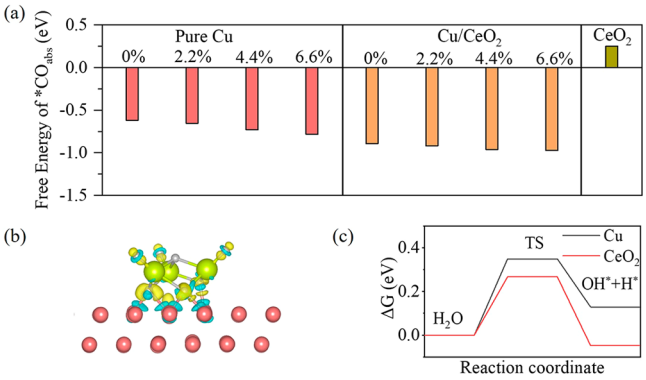

Figure 1. DFT calculation results. (a) Calculated *CO adsorption energies on standard Cu, stretched Cu, Cu/CeO_2, stretched Cu/CeO_2 interface, and CeO_2. (b) The electron density difference of the Cu/CeO_2 model. The electron accumulation and depletion are shown in yellow and blue, respectively. (c) The transition barrier investigation for H_2O dissociation on Cu (111) and CeO_2 (111).

Experimentally, the cubical Cu_2O/CeO_2 nanostructures were synthesized via a self-templating method, as illustrated in Figure 2a.[29] First, the Cu_2O nanocubes were obtained through a solvothermal reaction. Then they were subsequently used as sacrificial templates to react with Ce (IV) precursors subsequently, resulting in a thin layer of Cu_2O/CeO_2 shell, maximizing the exposed interface area. The ratio of Ce/Cu can be adjusted by changing the input amount of Ce (IV) precursors. The final catalysts were labeled as Cu_2O/CeO_2-0.09, Cu_2O/CeO_2-0.18, and Cu_2O/CeO_2-0.27 with the estimated Ce/Cu atomic ratios of 0.09, 0.18, and 0.27, respectively. Note that the Cu_2O and Cu_2O/CeO_2-x derived catalysts were labeled as Cu and Cu/CeO_2-x (x = 0.09, 0.18, 0.27), respectively. The pristine Cu_2O was used as a control sample for all characterizations and electrochemical measurements.

To obtain information concerning the crystalline structure, geometric feature, and chemical state of the synthesized catalysts, powder X-ray diffraction (XRD), scanning electron microscopy (SEM), and transmission electron microscopy (TEM) analysis were performed. The XRD pattern of Cu_2O/CeO_2-0.18 in Figure 2b confirmed that the heterostructure was composed of the cubic Cu_2O phase (JCPDS No. 65-3288) and fluorite CeO_2 phase (JCPDS No. 34-0394), and no diffraction peaks related to Cu or CuO phase were observed. Compared with the XRD patterns of the pure Cu_2O in Figure S3, the diffraction peaks of Cu_2O in Cu_2O/CeO_2-0.18 shifted toward the small-angle direction (Table S2), indicating the lattice expansion, which might be caused by the dissimilar interplanar spacing of CeO_2 (111) plane (d_{hkl} = 0.312 nm) in the outermost shell.[30]

The cubical shape of the synthesized nanostructures was revealed by both SEM and TEM images in Figures 2c,d and S4. After reacting with Ce (IV) precursors, the core/shell structure keeps the original cubic outline with increased surface roughness. Energy-dispersive X-ray spectroscopy

https://doi.org/10.1021/acsnano.2c08453
ACS Nano 2023, 17, 346−354

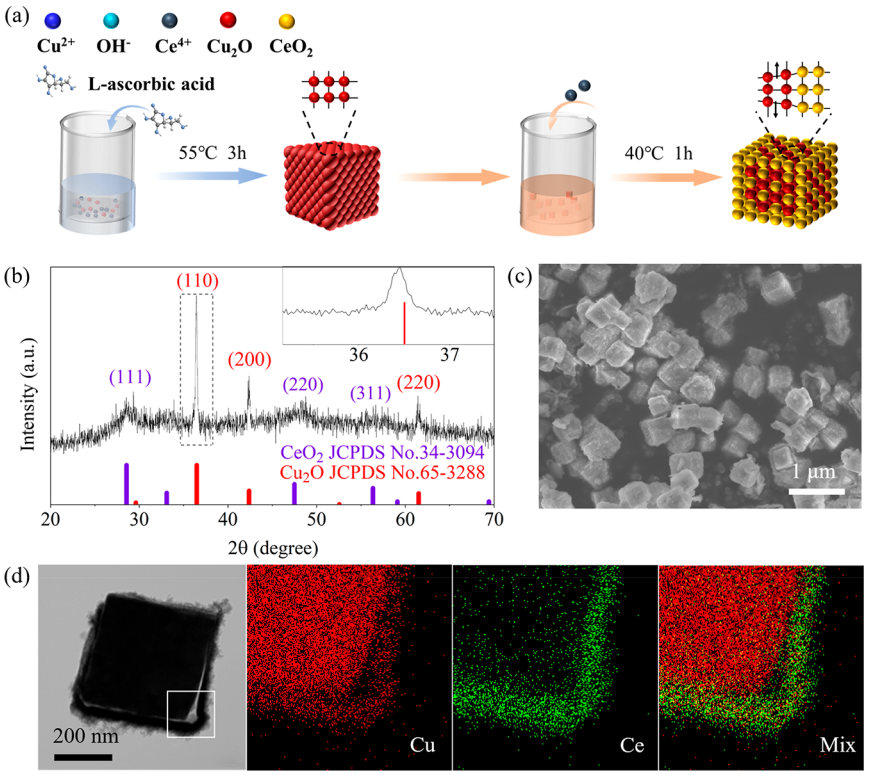

Figure 2. Synthesis and structural characterizations of a Cu_2O/CeO_2-0.18 core/shell nanostructure. (a) Synthetic scheme of electrocatalysts. (b) XRD pattern, (c) SEM and (d) TEM image, and EDS elemental maps, for the region marked by a white frame in (d).

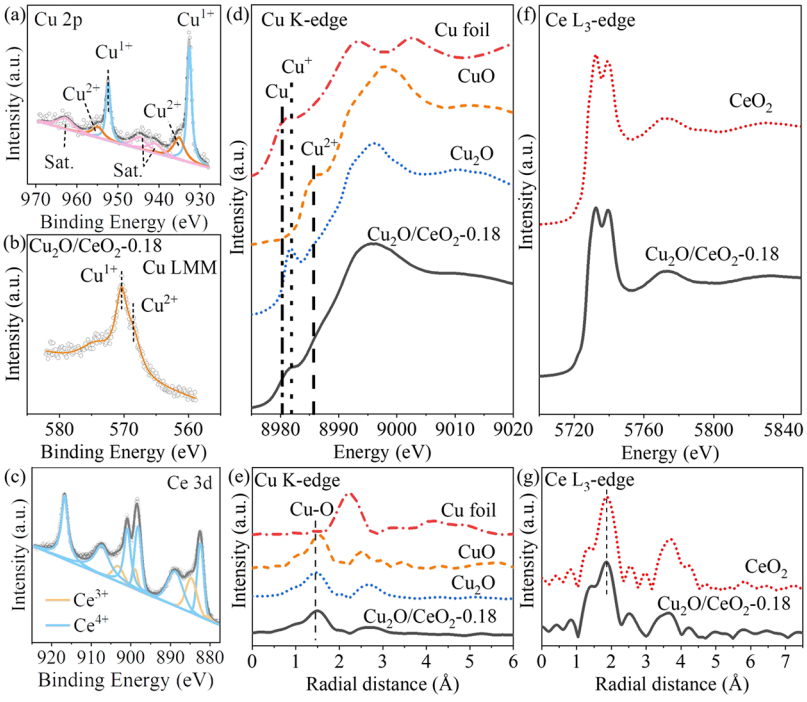

Figure 3. Chemical structure and state analysis of Cu_2O/CeO_2-0.18. (a) High-resolution XPS of Cu 2p. The scatter indicates the experimental data, and the solid lines correspond to the fitting. The blue curves represent Cu or Cu^+ states, the orange curves represent Cu^{2+} states, and the pink curves represent the satellite peaks. (b) Cu LMM of AES. The peak locations of different valence states were labeled. (c) High-resolution XPS of Ce 3d. The blue curves represent Ce^{4+} states, and the orange curves represent Ce^{3+} states. (d) XANES and (e) the corresponding FT of k^3-weighted EXAFS data of Cu K-edge. (f) XANES and (g) the corresponding FT of k^3-weighted EXAFS data of Ce L_3-edge. Note that the standard lines of CuO, Cu_2O, Cu foil, and CeO_2 were obtained from commercial samples.

(EDS) elemental mapping in Figure 2d illustrated a uniform spatial distribution of Cu and a Ce-rich shell. The atomic ratio of Cu to Ce is analyzed and shown in Table S3. The final structure is a cubic Cu_2O core with a thin Cu_2O/CeO_2 hybrid

https://doi.org/10.1021/acsnano.2c08453
ACS Nano 2023, 17, 346−354

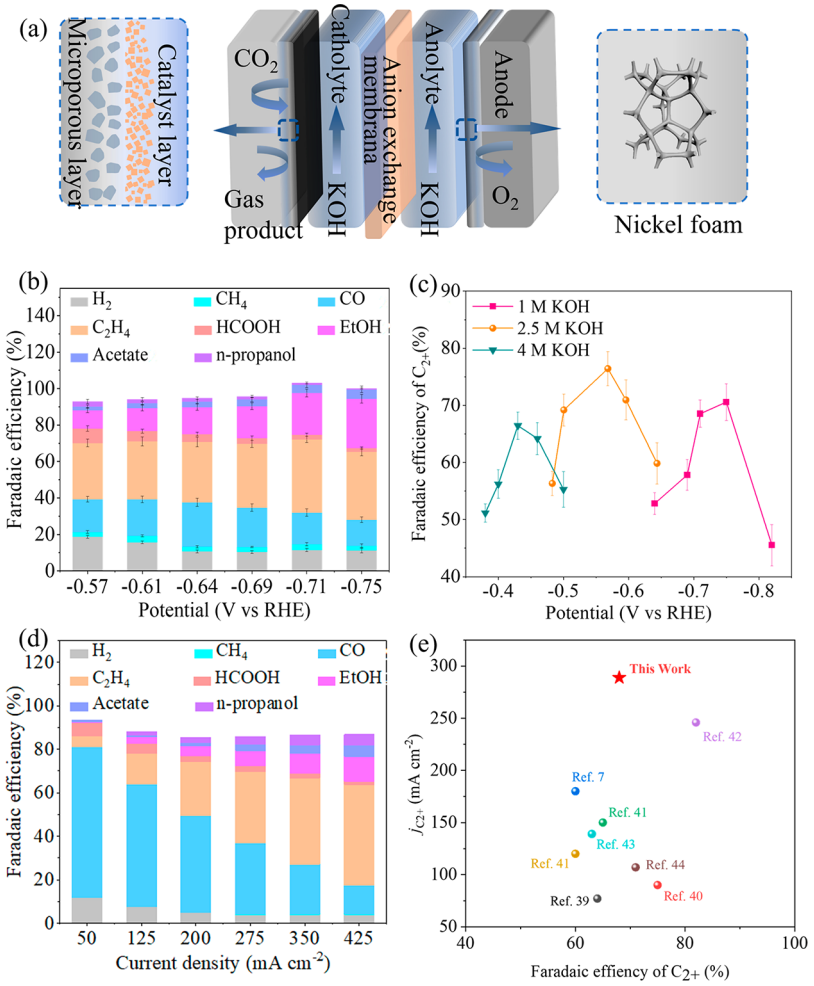

Figure 4. Electrocatalytic CO_2R performances. (a) Schematic illustration of the flow cell system. (b) FEs of all the products at different applied potentials for Cu_2O/CeO_2-0.18 in flow cell system. (c) FEs of C_{2+} products for Cu_2O/CeO_2-0.18 in KOH with different concentrations in flow cell system. (d) FEs of all the products at different applied current densities for Cu_2O/CeO_2-0.18 in the MEA system. (e) Comparison of CO_2R performance in the MEA system with various previous reported catalysts.

shell. The nanosized thickness of the shell enables the application of the core/shell structure for electrochemical use with limited conductivity losses due to the presence of the insulating ceria.

X-ray photoelectron spectroscopy (XPS) was used to analyze the surface chemical structure and valence state of the synthesized sample (Figure 3a–c). The survey XPS is shown in Figure S5, and the presence of Cu, Ce, and O elements was confirmed. Based on the high-resolution XPS of the Cu 2p spectrum of Cu_2O/CeO_2-0.18 in Figure 3a, a dominant valence state of Cu^0/Cu^+, was indicated by two prominent peaks located at 932.6 and 952.4 eV.[14] To further distinguish Cu^0 and Cu^+, the Auger electron spectroscopy (AES) measurement with higher energy resolution was performed. Cu LMM of AES in Figure 3b shows a strong peak at 570.4 eV related to Cu^{1+}, and no signal of Cu at 567.9 eV was observed. The weak peak at 568.6 eV corresponded to Cu^{2+}, which was also revealed in a Cu 2p spectrum at 934.8 and 953.8 eV accompanied by satellite peaks. These results help in interpreting the XPS results in terms of the presence of Cu^+, rather than Cu^0. These experimental findings are also in agreement with XRD, where no metallic Cu was detected for both Cu_2O and Cu_2O/CeO_2 series. The presence of Cu^{2+} might originate from the partial surface oxidation of Cu_2O when the catalysts were exposed to air.[14] The spectra of Ce 3d XPS in Figure 3c confirmed the coexistence of Ce^{3+} and Ce^{4+}, with two pairs of typical Ce^{3+} peaks and three pairs of Ce^{4+} peaks.[30] The relative content of two Ce states was evaluated by comparing the peak area (Table S4), and Ce^{4+} was the dominant state.

The chemical states of Cu and Ce were further characterized by X-ray absorption spectroscopy (XAS). As shown in Figure 3d, the X-ray absorption near-edge structure (XANES) of the Cu K-edge spectrum of Cu_2O/CeO_2-0.18 confirms the average Cu valency to be ~1. The Fourier-transformed (FT) extended X-ray absorption fine structure (EXAFS) spectra are shown in Figure 3e. The Cu–O coordination shell of Cu_2O/CeO_2-0.18 centered at ca. 1.50 Å shows a longer radial distance (1.91 Å) than that of Cu_2O (1.87 Å) at ca. 1.46, by quantitative EXAFS curve fitting (Figure S6 and Table S5). The stretched Cu–O bonds agreed with the enlarged interplanar spacing revealed by the XRD result. The XANES spectra of Ce L_3-edge and related FT of EXAFS spectra are shown in Figure 3f,g. Compared with the spectra of standard CeO_2, no distinguishable difference could be observed, indicating CeO_2 as the dominant phase in the shell.

The combination of XRD, EDS, XPS, and XAS allows us to conclude that the synthesized nanocube consisted of a Cu_2O

https://doi.org/10.1021/acsnano.2c08453
ACS Nano 2023, 17, 346–354

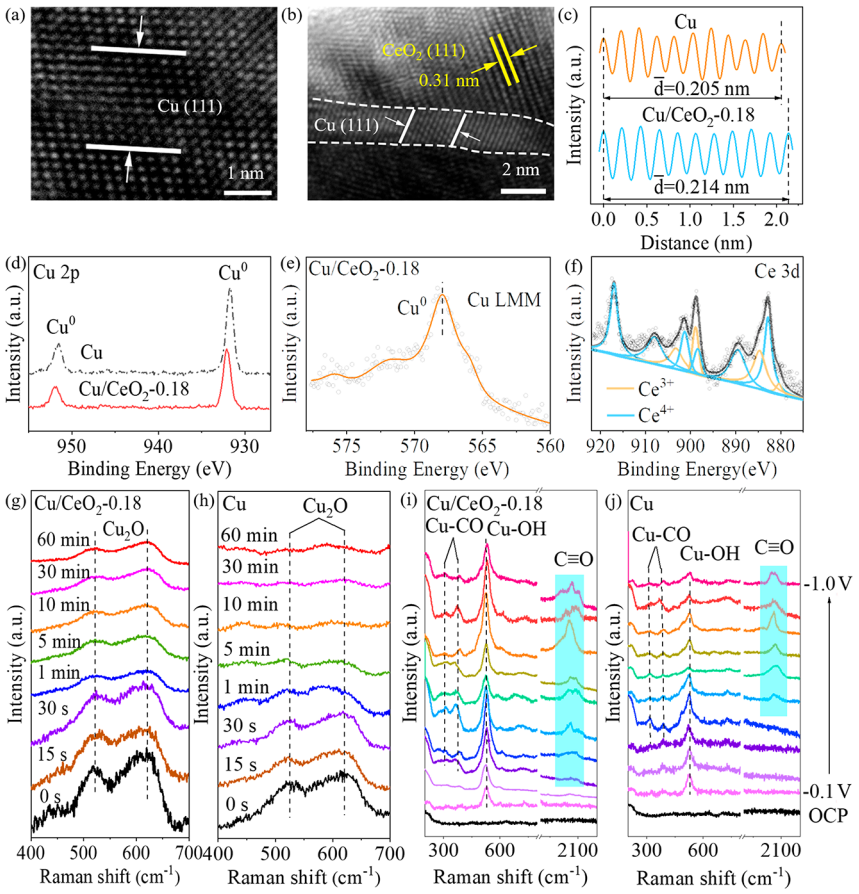

Figure 5. Crystal and chemical structure analysis of Cu_2O/CeO_2-0.18 after CO_2R. HRTEM image of (a) Cu_2O derived Cu and (b) Cu_2O/CeO_2-0.18 derived Cu/CeO_2. (c) The integrated pixel intensities of Cu (111) in two samples. (d) High-resolution XPS of Cu 2p. (e) Cu LMM of AES. (f) High-resolution XPS of Ce 3d. The blue curves represent Ce^{4+} states, and the orange curves represent Ce^{3+} states. Operando Raman spectra of Cu/CeO_2-0.18 (g) and Cu (h) evolution as a function of reaction time at open circuit potential (OCP). Operando Raman spectra of intermediates adsorption on Cu (i) Cu/CeO_2-0.18 and (j) Cu as a function of applied potentials. The vertical potential scale holds for both (i) and (j) panels.

core and a Cu_2O/CeO_2 shell. The dominant chemical states for Cu and Ce were Cu^+ and Ce^{4+}, respectively. Due to the larger lattice spacing of CeO_2, the Cu−O bond was stretched in the Cu_2O domain.

The electrocatalytic CO_2R was performed in a homemade flow cell system consisting of a catalyst-supported gas diffusion electrode (GDE), an Ag/AgCl reference electrode, a nickel foam counter electrode, and an anion exchange membrane, as shown in Figure 4a. KOH (1 M) was used as the electrolyte. The catalytic performance of three Cu_2O/CeO_2 heterostructures with different Cu/Ce ratios was compared against pristine Cu_2O. First, the linear sweep voltammetry (LSV) curves were measured to assess the CO_2R activity (Figure S7). Then, the CO_2R FEs of all catalysts and the partial current densities at different potentials were evaluated (Figures 4b,c, S8, S9). The gas products were analyzed by gas chromatography (GC), and the liquid products were analyzed by ^1H nuclear magnetic resonance (NMR) spectroscopy.

Figure S7 shows that the current density decreases when the ratio of CeO_2 increases, most likely because the low conductivity of CeO_2 hinders the electron transfer. Figure S8a (Table S6) and Figure 4b (Table S7) show the FE and the partial current densities of C_{2+} products at various potentials for all catalysts. Both the FE and the current density of Cu_2O/CeO_2-0.18 are higher than those of the other counterparts (Cu_2O, Cu_2O/CeO_2-0.09, and Cu_2O/CeO_2-0.27), suggesting their superior catalytic selectivity and activity. On Cu_2O/CeO_2-0.18, the highest C_{2+} Faradaic efficiency of ∼70.6% was obtained at −0.75 V vs RHE at a partial current density of 247 mA cm^{-2}. The FE of all products and the C_{2+} product formation rate of different catalysts at various potentials were evaluated in Figure 4b (Table S8), Figure S9 (Tables S9−S11), and Figure S10. The best performance was obtained in a potential range from −0.7 to −0.75 V vs RHE. At −0.75 V vs RHE, the C_{2+} products formation rate for Cu_2O/CeO_2-0.18 reached 795 μmol cm^{-2} h^{-1}, which was ∼1.4 times higher than that of Cu_2O (580 μmol cm^{-2} h^{-1}). The FE of H_2 at −0.75 V vs RHE for Cu_2O/CeO_2-0.18 was 10.1%, which was only 32% of that on Cu_2O (31.5%).

Increasing the KOH concentration can increase the selectivity toward C_{2+} products. However, the high hydroxide concentration would limit the CO_2 mass transport, resulting in an insufficient local CO_2 source.[31,32] For this reason, the CO_2R performance of Cu_2O/CeO_2-0.18 was evaluated in KOH electrolytes with different concentrations. In 2.5 M KOH, Cu_2O/CeO_2-0.18 can reach a C_{2+} FE of 76.4% and a half-cell power conversion efficiency (PCE) of 49.1% at −0.6 V vs RHE, whereas the selectivity lowered in both 1 and 4 M KOH (Figure 4c, Tables S12−S14 and Figures S11−S12). The operational stability of Cu_2O/CeO_2-0.18 at various KOH

https://doi.org/10.1021/acsnano.2c08453
ACS Nano 2023, 17, 346−354

concentrations is shown in Figure S13. The catalysts showed ≥3 h operational stability with a near-constant current density and C_{2+} FE in 1 and 2.5 M KOH, and ∼100 min stability in 4 M KOH. 85% ohmic *iR* drop correction was applied in each test. *R* values of different electrolytes were determined by EIS at open circuit voltages (Figure S14, Table S16). 2.5 M KOH is the optimum condition for C_{2+} production in our system.

In addition, we integrated Cu_2O/CeO_2-0.18 catalysts into a membrane electrode assembly (MEA) system, which shows a similar configuration to the industrial electrochemical catalytic system, to evaluate its performance. As shown in Figure 4d and Figure S15, a partial current density of 289 mA cm^{-2} was obtained at a full-cell potential of 3.7 V with a FE_{C2+} of ∼68%, which is much higher than that of the previous reported catalysts.[39−44]

We excluded the contribution of the electrochemical active surface area (ECSA) to the enhanced catalytic performance of Cu_2O/CeO_2-0.18 by the observation of higher ECSA-normalized current density on Cu_2O/CeO_2-0.18 than on the control (Figure S16).

To understand the origin of the high C_{2+} product selectivity, both Cu_2O and Cu_2O/CeO_2-0.18 were analyzed after CO_2R. Note that pure ceria did not produce C_{2+} products, and thus the $Ce^{3+/4+}$ species are not the active sites for C−C coupling (Figure S17).[5] High-resolution TEM (HRTEM) and elemental maps (Figure 5a−c and Figuress S18−S20) show that the catalysts preserved their cubic shape after catalysis, while the Cu_2O converted into metallic Cu. XRD results showed that all Cu_2O were reduced to Cu under the negative potential (Figure S19). The HRTEM image shows the intergrowth of Cu and CeO_2, and the interfacial regions consist of Cu and CeO_2 domains with connection edges along the (111) planes (Figure 5b). Note that the interplanar spacing of the Cu (111) plane is 0.205 nm in the pure Cu_2O-derived catalyst, and it increased to 0.214 nm in the Cu_2O/CeO_2-0.18 derived sample (Figures 5a−c and S20). Compared with the counterpart (Cu), the XRD peaks of Cu/CeO_2-0.18 show a slightly blue shift, and the full width of half-maximum enlarged slightly, which might be caused by the formation of the microstrain zone.[22] The distortion of Cu lattice in the heterostructure caused stretched lattice spacing, which would introduce tensile strains into the Cu domain.

The chemical state changes of catalysts after CO_2R were studied by XPS. High-resolution XPS of Cu 2p confirmed that Cu_2O was reduced to Cu (Figure 5d,e). Compared with the sample derived from Cu_2O, the peak of Cu in Cu/CeO_2-0.18 shifted 0.4 eV toward the high-energy direction (Figure 5d), indicating an electron loss from Cu.[30] The possible reason is that the incorporation of ceria induces deficient electron density around copper because the charge transfer between copper and ceria is spontaneous,[5] which is consistent with our DFT results. The high-resolution XPS of Ce 3d shows that the dominant chemical state of Ce is Ce^{4+} (Figure 5f and Table S4).

To monitor the structural evolution of catalysts during CO_2R, *in situ* Raman with a 633 nm excitation wavelength was applied to Cu_2O and Cu_2O/CeO_2-0.18 samples. At an open circuit potential (OCP), two typical Raman peaks at 525 and 625 cm^{-1} attributed to the Γ^{+}_{25} and $\Gamma^{-}_{12}+\Gamma^{+}_{25}$ phonon modes of Cu_2O were observed in the two catalysts (Figures 5g,h and S21).[16,33] The Raman signals at 465 cm^{-1} assigned to the F_{2g} vibration of CeO_2 were not observed, probably due to the low content and the small Raman scattering cross-section of CeO_2.[5] After the negative potential (−0.7 V vs RHE) was applied, these Raman signals of Cu_2O disappeared within 10 min for the pure Cu_2O due to the rapid and complete reduction of Cu_2O to Cu. However, the characteristic Cu_2O modes of Cu_2O/CeO_2-0.18 were retained for at least 60 min, suggesting the enhanced stability of Cu^{+} under reaction conditions in the core/shell sample. Raman results indicate that the Cu_2O in the heterostructure is more resistant to cathodic reduction due to the interaction between Cu_2O and CeO_2, and the slow reduction of Cu^{+} species favors the formation of strained copper domains. Considering the low current density during *in situ* Raman operation, the *ex-situ* Raman studies of Cu_2O/CeO_2-0.18 were carried out after 30 min operation in the flow-cell system. As shown in Figure 5i,j, no signal of Cu_2O was observed after reacting for 30 min under a current density of 350 mA/cm^2, indicating that all Cu_2O was reduced to copper. However, we cannot exclude a trace amount of Cu^{+} residual in the catalysts below the detection limit of Raman spectroscopy.

Raman signals can also provide information on adsorbed reaction intermediates. The *CO binding was probed directly in our measurements. The catalysts were prereduced via operating in a flow-cell system at −0.75 V vs RHE for half an hour, to obtain the complete reduction of the original Cu_2O phase. Then, the electrodes were rinsed with deionized water and dried under N_2. The binding of *CO was probed by Raman spectroscopy at applied potentials starting from zero to more negative values. At the negative potentials, the peaks at 300−390 cm^{-1} related to the restricted rotation of adsorbed *CO on Cu or Cu−CO stretching, and 2000−2078 cm^{-1} corresponding to the C≡O stretching (Figure 5i,j) are observed.[33] The Raman features of C≡O appeared at −0.3 V vs RHE and −0.4 V vs RHE for Cu_2O/CeO_2-0.18 and Cu_2O derived samples, respectively. Taking into account that these two samples have similar ECSAs, the Raman results indicate a lower formation energy barrier of *CO on the former. Moreover, the strong peak intensity of *CO on Cu_2O/CeO_2-0.18 and the red shift of peak position compared with that on Cu_2O demonstrated a higher surface coverage and stronger adsorption of *CO on the sample derived from Cu_2O/CeO_2-0.18, which facilitated subsequently CO coupling to form C_{2+} products.[21] Moreover, the Raman spectrum of Cu_2O/CeO_2-0.18 has a more pronounced peak at ∼530 cm^{-1}, corresponding to the stretching vibration of Cu−OH, indicating high *OH coverage.[5] Figure S22 exhibits *in situ* ATR-SEIRAS of Cu_2O/CeO_2-0.18 and Cu_2O derived catalysts. The peaks at 2120 cm^{-1} are associated with linear-bond *CO.[34] Under the same applied voltage, the peak intensities of Cu/CeO_2-0.18 are stronger than that of Cu, indicating a higher *CO coverage.

To confirm the chemical states of the catalysts after CO_2R, reaction time-dependent XPS measurements were carried out (Figure S23). The chemical state of Ce exhibits no significant change during the reduction reaction, whereas the state of Cu is gradually reduced from +1 to 0 as the reaction time goes on. Moreover, in situ Raman also detected the reduction of Cu_2O (Figure 5g,h). So the active sites of our catalysts should be Cu^0 rather than Cu^{+} sites.

In a previous report, a CeO_2 matrix was used to protect the high valent $Cu^{1+/2+}$ sites from reduction.[27] However, we found that our Cu_2O/CeO_2-0.18 was completely reduced to metallic Cu during CO_2R as confirmed by in situ Raman (Figure 5g,h), time-dependent XPS (Figure S23), and XRD (Figure S19).

https://doi.org/10.1021/acsnano.2c08453
ACS Nano 2023, 17, 346−354

Thus, Cu^+ sites in our catalysts did not play a significant role in promoting C_{2+} production.

In this work, the strain effect in copper domains caused by CeO_2 is considered for enhanced C_{2+} selectivity. Based on Nørskov's "d-band-center model",[35−37] the tensile strain causes lattice expansion, which reduces orbital overlap in transition metal atoms, resulting in an upshifted d-band center and narrowed bandwidth. Thus, d-states with higher energy promote a stronger interaction between Cu atoms with adsorbates.[21,38] The strengthen *CO binding induced by tensile strain is favorable for C−C coupling through the dimerization of *CO, leading to enhanced C_{2+} selectivity.

CONCLUSION

In summary, we investigated the effect of strain on the Cu/CeO_2 interface to CO_2R. And we have demonstrated that constructing the Cu/ceria interface can facilitate the C_{2+} selectivity and activity during CO_2R. Tensile strain in the Cu domain caused by a lattice mismatch was found to strengthen the adsorption of *CO. Spectroscopic analysis and DFT calculations revealed that the charge transfer from Cu to ceria retards the reduction of Cu_2O, resulting in electron deficient copper sites which further stabilize *CO and promote C−C coupling. Moreover, the presence of CeO_2 sites favors water dissociation, which could accelerate CO_2 conversion by feeding sufficient protons. In a flow-cell system with 2.5 M KOH as the electrolyte, the optimized catalysts exhibited a C_{2+} FE of 76.4%. The strain effect revealed in this work is critical for fully understanding the origin of promoted selectivity in the copper/ceria system and proposing a design strategy for improving C_{2+} selectivity.

ASSOCIATED CONTENT

Supporting Information

The Supporting Information is available free of charge at https://pubs.acs.org/doi/10.1021/acsnano.2c08453.

Materials, synthesis, characterization methods, calculations, and additional experimental results (PDF)

AUTHOR INFORMATION

Corresponding Author

Hongyan Liang − *School of Materials Science and Engineering and Key Laboratory of Efficient Utilization of Low and Medium Grade Energy, Ministry of Education, Tianjin University, Tianjin 300350, P. R. China;* orcid.org/0000-0001-6623-6946; Email: hongyan.liang@tju.edu.cn

Authors

Haibin Wang − *School of Materials Science and Engineering and Key Laboratory of Efficient Utilization of Low and Medium Grade Energy, Ministry of Education, Tianjin University, Tianjin 300350, P. R. China;* orcid.org/0000-0002-2219-0963

Hao Zhang − *Institute of Functional Nano and Soft Materials (FUNSOM), Soochow University, Suzhou 215123, P. R. China;* orcid.org/0000-0003-2300-1404

Yan Huang − *School of Materials Science and Engineering and Key Laboratory of Efficient Utilization of Low and Medium Grade Energy, Ministry of Education, Tianjin University, Tianjin 300350, P. R. China*

Haiyu Wang − *School of Materials Science and Engineering, Tianjin University, Tianjin 300350, P. R. China*

Adnan Ozden − *Department of Mechanical and Industrial Engineering, University of Toronto, Toronto, Ontario M5S 3G8, Canada;* orcid.org/0000-0002-6924-1967

Kaili Yao − *School of Materials Science and Engineering, Tianjin University, Tianjin 300350, P. R. China*

Huamin Li − *School of Materials Science and Engineering, Tianjin University, Tianjin 300350, P. R. China*

Qianying Guo − *School of Materials Science and Engineering, Tianjin University, Tianjin 300350, P. R. China*

Yongchang Liu − *School of Materials Science and Engineering and State Key Lab of Hydraulic Engineering Simulation and Safety, Tianjin University, Tianjin 300350, P. R. China*

Alberto Vomiero − *Division of Materials Science, Department of Engineering Sciences and Mathematics, Luleå University of Technology, 97187 Luleå, Sweden; Department of Molecular Sciences and Nanosystems, Ca' Foscari University of Venice, 30172 Venezia Mestre, Italy;* orcid.org/0000-0003-2935-1165

Yuhang Wang − *Institute of Functional Nano and Soft Materials (FUNSOM), Soochow University, Suzhou 215123, P. R. China;* orcid.org/0000-0001-5336-5183

Zhao Qian − *Key Laboratory of Liquid−Solid Structural Evolution and Processing of Materials, Ministry of Education Shandong University, Jinan 250061, P. R. China*

Jun Li − *Frontiers Science Center for Transformative Molecules, Shanghai Jiao Tong University, Shanghai 200240, China*

Ziyun Wang − *School of Chemical Sciences, the University of Auckland, Auckland 1010, New Zealand;* orcid.org/0000-0002-2817-8367

Xuhui Sun − *Institute of Functional Nano and Soft Materials (FUNSOM), Soochow University, Suzhou 215123, P. R. China;* orcid.org/0000-0003-0002-1146

Complete contact information is available at: https://pubs.acs.org/10.1021/acsnano.2c08453

Notes

The authors declare no competing financial interest.

ACKNOWLEDGMENTS

This work was supported by the National Natural Science Foundation of China (NSFC Nos. 51771132, 52204320). H.Z., Y.H.W. and X.H.S. acknowledge the Suzhou Key Laboratory of Functional Nano & Soft Materials, the Collaborative Innovation Center of Suzhou Nano Science & Technology, the 111 Project, and the Joint International Research Laboratory of Carbon-Based Functional Materials and Devices. The authors also thank the BL14W1 XAFS beamline of SSRF for providing beamtime.

REFERENCES

(1) Sisler, J.; Khan, S.; Ip, A. H.; Schreiber, M. W.; Jaffer, S. A.; Bobicki, E. R.; Dinh, C. T.; Sargent, E. H. Ethylene Electrosynthesis: A Comparative Techno-economic Analysis of Alkaline vs Membrane Electrode Assembly vs CO_2-CO-C_2H_4 Tandems. *ACS Energy Lett.* **2021**, *6* (3), 997−1002.

(2) Gao, D. F.; Aran-Ais, R. M.; Jeon, H. S.; Roldan Cuenya, B. Rational catalyst and electrolyte design for CO_2 electroreduction towards multicarbon products. *Nature Catalysis* **2019**, *2* (3), 198−210.

(3) Gao, D. F.; Sinev, I.; Scholten, F.; Aran-Ais, R. M.; Divins, N. J.; Kvashnina, K.; Timoshenko, J.; Roldan Cuenya, B. Selective CO_2 Electroreduction to Ethylene and Multicarbon Alcohols via Electro-

lyte-Driven Nanostructuring. *Angew. Chem. Int. Edit* **2019**, *58* (47), 17047−17053.
(4) Todorova, T. K.; Schreiber, M. W.; Fontecave, M. Mechanistic Understanding of CO_2 Reduction Reaction (CO_2RR) Toward Multicarbon Products by Heterogeneous Copper-Based Catalysts. *ACS Catal.* **2020**, *10* (3), 1754−1768.
(5) Lee, C. W.; Shin, S. J.; Jung, H.; Nguyen, D. L. T.; Lee, S. Y.; Lee, W. H.; Won, D. H.; Kim, M. G.; Oh, H. S.; Jang, T.; Kim, H.; Min, B. K.; Hwang, Y. J. Metal-Oxide Interfaces for Selective Electrochemical C-C Coupling Reactions. *ACS Energy Lett.* **2019**, *4* (9), 2241−2248.
(6) Kuhl, K. P.; Hatsukade, T.; Cave, E. R.; Abram, D. N.; Kibsgaard, J.; Jaramillo, T. F. Electrocatalytic conversion of carbon dioxide to methane and methanol on transition metal surfaces. *J. Am. Chem. Soc.* **2014**, *136* (40), 14107−13.
(7) Wang, Y. H.; Wang, Z. Y.; Dinh, C. T.; Li, J.; Ozden, A.; Kibria, M. G.; Seifitokaldani, A.; Tan, C. S.; Gabardo, C. M.; Luo, M. C.; Zhou, H.; Li, F. W.; Lum, Y.; McCallum, C.; Xu, Y.; Liu, M. X.; Proppe, A.; Johnston, A.; Todorovic, P.; Zhuang, T. T.; Sinton, D.; Kelley, S. O.; Sargent, E. H. Catalyst synthesis under CO_2 electroreduction favours faceting and promotes renewable fuels electrosynthesis. *Nature Catalysis* **2020**, *3* (2), 98−106.
(8) Zhong, D. Z.; Zhao, Z. J.; Zhao, Q.; Cheng, D. F.; Liu, B.; Zhang, G.; Deng, W. Y.; Dong, H.; Zhang, L.; Li, J. K.; Li, J. P.; Gong, J. L. Coupling of Cu(100) and (110) Facets Promotes Carbon Dioxide Conversion to Hydrocarbons and Alcohols. *Angew. Chem. Int. Edit* **2021**, *60* (9), 4879−4885.
(9) Jeon, H. S.; Timoshenko, J.; Rettenmaier, C.; Herzog, A.; Yoon, A.; Chee, S. W.; Oener, S.; Hejral, U.; Haase, F. T.; Cuenya, B. R. Selectivity Control of Cu Nanocrystals in a Gas-Fed Flow Cell through CO_2 Pulsed Electroreduction. *J. Am. Chem. Soc.* **2021**, *143* (19), 7578−7587.
(10) Zhang, B. X.; Zhang, J. L.; Hua, M. L.; Wan, Q.; Su, Z. Z.; Tan, X. N.; Liu, L. F.; Zhang, F. Y.; Chen, G.; Tan, D. X.; Cheng, X. Y.; Han, B. X.; Zheng, L. R.; Mo, G. Highly Electrocatalytic Ethylene Production from CO_2 on Nanodefective Cu Nanosheets. *J. Am. Chem. Soc.* **2020**, *142* (31), 13606−13613.
(11) Kim, T.; Palmore, G. T. R. A scalable method for preparing Cu electrocatalysts that convert CO_2 into C_{2+} products. *Nat. Commun.* **2020**, *11* (1), 3622.
(12) Zhou, Y. S.; Che, F. L.; Liu, M.; Zou, C. Q.; Liang, Z. Q.; De Luna, P.; Yuan, H. F.; Li, J.; Wang, Z. Q.; Xie, H. P.; Li, H. M.; Chen, P. N.; Bladt, E.; Quintero-Bermudez, R.; Sham, T. K.; Bals, S.; Hofkens, J.; Sinton, D.; Chen, G.; Sargent, E. H. Dopant-induced electron localization drives CO_2 reduction to C_2 hydrocarbons. *Nat. Chem.* **2018**, *10* (9), 974−980.
(13) Zhang, W.; Huang, C. Q.; Xiao, Q.; Yu, L.; Shuai, L.; An, P. F.; Zhang, J.; Qiu, M.; Ren, Z. F.; Yu, Y. Atypical Oxygen-Bearing Copper Boosts Ethylene Selectivity toward Electrocatalytic CO_2 Reduction. *J. Am. Chem. Soc.* **2020**, *142* (26), 11417−11427.
(14) Yao, K. L.; Xia, Y. J.; Li, J.; Wang, N.; Han, J. R.; Gao, C. C.; Han, M.; Shen, G. Q.; Liu, Y. C.; Seifitokaldani, A.; Sun, X. H.; Liang, H. Y. Metal-organic framework derived copper catalysts for CO_2 to ethylene conversion. *J. Mater. Chem. A* **2020**, *8* (22), 11117−11123.
(15) Zhuang, T. T.; Pang, Y. J.; Liang, Z. Q.; Wang, Z. Y.; Li, Y.; Tan, C. S.; Li, J.; Dinh, C. T.; De Luna, P.; Hsieh, P. L.; Burdyny, T.; Li, H. H.; Liu, M. X.; Wang, Y. H.; Li, F. W.; Proppe, A.; Johnston, A.; Nam, D. H.; Wu, Z. Y.; Zheng, Y. R.; Ip, A. H.; Tan, H. R.; Chen, L. J.; Yu, S. H.; Kelley, S. O.; Sinton, D.; Sargent, E. H. Copper nanocavities confine intermediates for efficient electrosynthesis of C_3 alcohol fuels from carbon monoxide. *Nature Catalysis* **2018**, *1* (12), 946−951.
(16) Yang, P. P.; Zhang, X. L.; Gao, F. Y.; Zheng, Y. R.; Niu, Z. Z.; Yu, X. X.; Liu, R.; Wu, Z. Z.; Qin, S.; Chi, L. P.; Duan, Y.; Ma, T.; Zheng, X. S.; Zhu, J. F.; Wang, H. J.; Gao, M. R.; Yu, S. H. Protecting Copper Oxidation State via Intermediate Confinement for Selective CO2 Electroreduction to C_{2+} Fuels. *J. Am. Chem. Soc.* **2020**, *142* (13), 6400−6408.
(17) Gabardo, C. M.; Seifitokaldani, A.; Edwards, J. P.; Dinh, C.-T.; Burdyny, T.; Kibria, M. G.; O'Brien, C. P.; Sargent, E. H.; Sinton, D. Combined high alkalinity and pressurization enable efficient CO_2 electroreduction to CO. *Energ Environ. Sci.* **2018**, *11* (9), 2531−2539.
(18) Wang, X.; Liu, C.; Gao, C.; Yao, K.; Masouleh, S. S. M.; Berte, R.; Ren, H.; Menezes, L. S.; Cortes, E.; Bicket, I. C.; Wang, H.; Li, N.; Zhang, Z.; Li, M.; Xie, W.; Yu, Y.; Fang, Y.; Zhang, S.; Xu, H.; Vomiero, A.; Liu, Y.; Botton, G. A.; Maier, S. A.; Liang, H. Self-Constructed Multiple Plasmonic Hotspots on an Individual Fractal to Amplify Broadband Hot Electron Generation. *ACS Nano* **2021**, *15* (6), 10553−10564.
(19) Chen, Z.; Zhang, X.; Lu, G. Overpotential for CO_2 electroreduction lowered on strained penta-twinned Cu nanowires. *Chem. Sci.* **2015**, *6* (12), 6829−6835.
(20) Han, M.; Wang, N.; Zhang, B.; Xia, Y. J.; Li, J.; Han, J. R.; Yao, K. L.; Gao, C. C.; He, C. N.; Liu, Y. C.; Wang, Z. M.; Seifitokaldani, A.; Sun, X. H.; Liang, H. Y. High-Valent Nickel Promoted by Atomically Embedded Copper for Efficient Water Oxidation. *ACS Catal.* **2020**, *10* (17), 9725−9734.
(21) Kim, T.; Kumar, R. E.; Brock, J. A.; Fullerton, E. E.; Fenning, D. P. How Strain Alters CO_2 Electroreduction on Model Cu(001) Surfaces. *ACS Catal.* **2021**, *11* (11), 6662−6671.
(22) Xia, Z. H.; Guo, S. J. Strain engineering of metal-based nanomaterials for energy electrocatalysis. *Chem. Soc. Rev.* **2019**, *48* (12), 3265−3278.
(23) Khorshidi, A.; Violet, J.; Hashemi, J.; Peterson, A. A. How strain can break the scaling relations of catalysis. *Nature Catalysis* **2018**, *1* (4), 263−268.
(24) Li, Y. W.; Sun, Q. Recent Advances in Breaking Scaling Relations for Effective Electrochemical Conversion of CO_2. *Adv. Energy Mater.* **2016**, *6* (17), 1600463.
(25) Clark, E. L.; Hahn, C.; Jaramillo, T. F.; Bell, A. T. Electrochemical CO_2 Reduction over Compressively Strained CuAg Surface Alloys with Enhanced Multi-Carbon Oxygenate Selectivity. *J. Am. Chem. Soc.* **2017**, *139* (44), 15848−15857.
(26) Vasileff, A.; Xu, C. C.; Jiao, Y.; Zheng, Y.; Qiao, S. Z. Surface and Interface Engineering in Copper-Based Bimetallic Materials for Selective CO_2 Electroreduction. *Chem-Us* **2018**, *4* (8), 1809−1831.
(27) Zhou, X. L.; Shan, J. Q.; Chen, L.; Xia, B. Y.; Ling, T.; Duan, J. J.; Jiao, Y.; Zheng, Y.; Qiao, S. Z. Stabilizing Cu^{2+} Ions by Solid Solutions to Promote CO_2 Electroreduction to Methane. *J. Am. Chem. Soc.* **2022**, *144* (5), 2079−2084.
(28) Luo, M. C.; Wang, Z. Y.; Li, Y. G. C.; Li, J.; Li, F. W.; Lum, Y. W.; Nam, D. H.; Chen, B.; Wicks, J.; Xu, A. N.; Zhuang, T. T.; Leow, W. R.; Wang, X.; Dinh, C. T.; Wang, Y.; Wang, Y. H.; Sinton, D.; Sargent, E. H. Hydroxide promotes carbon dioxide electroreduction to ethanol on copper via tuning of adsorbed hydrogen. *Nat. Commun.* **2019**, *10*, 5814.
(29) Bao, H. Z.; Zhang, Z. H.; Hua, Q.; Huang, W. X. Compositions, Structures, and Catalytic Activities of CeO_2@Cu_2O Nanocomposites Prepared by the Template-Assisted Method. *Langmuir* **2014**, *30* (22), 6427−6436.
(30) Varandili, S. B.; Huang, J. F.; Oveisi, E.; De Gregorio, G. L.; Mensi, M.; Strach, M.; Vavra, J.; Gadiyar, C.; Bhowmik, A.; Buonsanti, R. Synthesis of Cu/CeO_{2-x} Nanocrystalline Heterodimers with Interfacial Active Sites To Promote CO_2 Electroreduction. *ACS Catal.* **2019**, *9* (6), 5035−5046.
(31) Li, J.; Wang, Z.; McCallum, C.; Xu, Y.; Li, F.; Wang, Y.; Gabardo, C. M.; Dinh, C. T.; Zhuang, T. T.; Wang, L.; Howe, J. Y.; Ren, Y.; Sargent, E. H.; Sinton, D. Constraining CO coverage on copper promotes high-efficiency ethylene electroproduction. *Nat. Catal* **2019**, *2*, 1124−1131.
(32) Dinh, C.-T.; Burdyny, T.; Kibria, M. G.; Seifitokaldani, A.; Gabardo, C. M.; Garcia de Arquer, F. P.; Kiani, A.; Edwards, J. P.; De Luna, P.; Bushuyev, O. S.; Zou, C.; Quintero-Bermudez, R.; Pang, Y.; Sinton, D.; Sargent, E. H. CO_2 electroreduction to ethylene via hydroxide-mediated copper catalysis at an abrupt interface. *Science* **2018**, *360* (6390), 783−787.

https://doi.org/10.1021/acsnano.2c08453
ACS Nano 2023, 17, 346−354

(33) Yan, X. P.; Chen, C. J.; Wu, Y. H.; Liu, S. J.; Chen, Y. Z.; Feng, R. J.; Zhang, J.; Han, B. X. Efficient electroreduction of CO_2 to C_{2+} products on CeO_2 modified CuO. *Chem. Sci.* **2021**, *12* (19), 6638−6645.
(34) Zhang, G.; Zhao, Z.-J.; Cheng, D.; Li, H.; Yu, J.; Wang, Q.; Gao, H.; Guo, J.; Wang, H.; Ozin, G. A.; Wang, T.; Gong, J. Efficient CO_2 electroreduction on facet-selective copper films with high conversion rate. *Nat. Commun.* **2021**, *12*, 5745.
(35) Nørskov, J. K.; Abild-Pedersen, F.; Studt, F.; Bligaard, T. Density functional theory in surface chemistry and catalysis. *Proc. Natl. Acad. Sci. U.S.A.* **2011**, *108* (3), 937−943.
(36) Mavrikakis, M.; Hammer, B.; Nørskov, J. K. Effect of Strain on the Reactivity of Metal Surfaces. *Phys. Rev. Lett.* **1998**, *81*, 2819.
(37) Luo, M.; Guo, S. Strain-controlled electrocatalysis on multimetallic nanomaterials. *Nat. Rev. Mater.* **2017**, *2*, 17059.
(38) Jansonius, R. P.; Reid, L. M.; Virca, C. N.; Berlinguette, C. P. Strain Engineering Electrocatalysts for Selective CO_2 Reduction. *ACS Energy Lett.* **2019**, *4* (4), 980−986.
(39) Li, F.; Thevenon, A.; Rosas-Hernandez, A.; Wang, Z.; Li, Y.; Gabardo, C. M.; Ozden, A.; Dinh, C. T.; Li, J.; Wang, Y.; Edwards, J. P.; Xu, Y.; McCallum, C.; Tao, L.; Liang, Z.-Q.; Luo, M.; Wang, X.; Li, H.; O'Brien, C. P.; Tan, C.-S.; Nam, D.-H.; Quintero-Bermudez, R.; Zhuang, T.-T.; Li, Y. C.; Han, Z.; Britt, R. D.; Sinton, D.; Agapie, T.; Peters, J. C.; Sargent, E. H. Molecular tuning of CO_2-to-ethylene conversion. *Nature* **2020**, *577*, 509−513.
(40) Li, F.; Li, Y. C.; Wang, Z.; Li, J.; Nam, D. H.; Lum, Y.; Luo, M.; Wang, X.; Ozden, A.; Hung, S. F.; Chen, B.; Wang, Y.; Wicks, J.; Xu, Y.; Li, Y.; Gabardo, C. M.; Dinh, C. T.; Wang, Y.; Zhuang, T. T.; Sinton, D.; Sargent, E. H. Cooperative CO_2-to-ethanol conversion via enriched intermediates at molecule−metal catalyst interfaces. *Nature* **2020**, *3*, 75−82.
(41) Gabardo, C. M.; O'Brien, C. P.; Edwards, J. P.; McCallum, C.; Xu, Y.; Dinh, C. T.; Li, J.; Sargent, E. H.; Sinton, D. Continuous Carbon Dioxide Electroreduction to Concentrated Multi-carbon Products Using a Membrane Electrode Assembly. *Joule* **2019**, *3* (11), 2777−2791.
(42) Li, J.; Ozden, A.; Wan, M.; Hu, Y.; Li, F.; Wang, Y.; Zamani, R. R.; Ren, D.; Wang, Z.; Xu, Y.; Nam, D. H.; Wicks, J.; Chen, B.; Wang, X.; Luo, M.; Graetzel, M.; Che, F.; Sargent, E. H.; Sinton, D. Silica-copper catalyst interfaces enable carbon-carbon coupling towards ethylene electrosynthesis. *Nat. Commum* **2021**, *12*, 2808.
(43) Ozden, A.; Li, F.; Garcıa de Arquer, F. P.; Rosas-Hernandez, A.; Thevenon, A.; Wang, Y.; Hung, S.-F.; Wang, X.; Chen, B.; Li, J.; Wicks, J.; Luo, M.; Wang, Z.; Agapie, T.; Peters, J. C.; Sargent, E. H.; Sinton, D. High-Rate and Efficient Ethylene Electrosynthesis Using a Catalyst/Promoter/Transport Layer. *ACS Energy Lett.* **2020**, *5* (9), 2811−2818.
(44) Kim, J. Y.; Hong, D.; Lee, J. C.; Kim, H. G.; Lee, S.; Shin, S.; Kim, B.; Lee, H.; Kim, M.; Oh, J.; Lee, G. D.; Nam, D. H.; Joo, Y. C. Quasi-graphitic carbon shell-induced Cu confinement promotes electrocatalytic CO_2 reduction toward C_{2+} products. *Nat. Commun.* **2021**, *12*, 3765.

https://doi.org/10.1021/acsnano.2c08453
ACS Nano 2023, 17, 346−354